# On the Effects of Surface Roughness on Boundary Layer Transition

Meelan Choudhari, Fei Li, Chau-Lyan Chang
*NASA Langley Research Center, Hampton, VA 23681*

Jack Edwards
*North Carolina State University, Raleigh, NC 27695*

**Surface roughness can influence laminar-turbulent transition in many different ways. This paper outlines selected analyses performed at the NASA Langley Research Center, ranging in speed from subsonic to hypersonic Mach numbers and highlighting the beneficial as well as adverse roles of the surface roughness in technological applications. The first theme pertains to boundary-layer tripping on the forebody of a hypersonic airbreathing configuration via a spanwise periodic array of trip elements, with the goal of understanding the physical mechanisms underlying roughness-induced transition in a high-speed boundary layer. The effect of an isolated, finite amplitude roughness element on a supersonic boundary layer is considered next. The other set of flow configurations examined herein corresponds to roughness based laminar flow control in subsonic and supersonic swept wing boundary layers. A common theme to all of the above configurations is the need to apply higher fidelity, physics based techniques to develop reliable predictions of roughness effects on laminar-turbulent transition.**

## I. INTRODUCTION

Surface roughness is known to have a substantial impact on boundary-layer transition and, hence, on the aerodynamic and/or aerothermodynamic predictions for flight vehicles across a wide range of Mach numbers. Small amplitude roughness over the appropriate range of surface locations may serve as a catalyst during the excitation of traveling wave instabilities due to free-stream unsteadiness, or act as a direct source of stationary vortex instabilities such as Gortler vortices and stationary crossflow modes. A striking example of the effect of roughness-induced receptivity on transition has been documented in [1], where transition was noted to move from between 25 to 30 percent chord to 80 percent chord when the painted leading edge was polished so as to reduce the roughness amplitude from 1.0 μm rms (3.8 μm average peak-to-peak) to 0.3 μm rms (2.2 μm average peak-to-peak). A recently proposed concept for transition control over swept aerodynamic surfaces involves the use of distributed roughness elements (DREs) near the leading edge [1, 2]. The DREs excite subdominant stationary crossflow modes that are not strong enough to cause transition on their own but can modify the underlying basic state so as to reduce the growth of the linearly most unstable crossflow modes.

Roughness at intermediate heights can further lead to a substantial modification of the underlying boundary layer and also scatter any incoming instability waves, so as to exert an overall impact on the growth characteristics of the boundary layer perturbations (see, e.g., [3]). A roughness strip producing a sufficiently large perturbation in surface height is often employed as a means to induce earlier transition in a laminar boundary layer. In certain other cases, the presence of unavoidable variations in surface geometry leads to unintended tripping of the boundary layer. The detailed physical mechanisms associated with roughness-induced tripping are not fully understood yet. In incompressible boundary layers, however, the earlier onset of transition behind discrete roughness elements may be linked to a spontaneous onset of vortex shedding behind the element [4]. On the other hand, there is reason to believe that the mechanism of laminar-turbulent transition due to distributed surface roughness may be related to a transient but large growth of linearly stable perturbations excited by the surface roughness [5]. For additional information pertaining to roughness effects on transition, the reader is referred to [6, 7].

This paper summarizes a select set of recent investigations involving the computations of roughness effects on boundary layer transition. For more complete descriptions of these studies, the reader is directed to Refs. [8–11]. Boundary-layer tripping mechanisms associated with spanwise periodic and isolated roughness elements in a high-speed boundary layer are discussed in Section 2. Section 3 is devoted to high fidelity transition analyses for the delay of crossflow transition in swept wing boundary layers using distributed roughness elements (DREs) near the leading edge. Because the transition delay via DREs is achieved via nonlinear effects associated with artificially

seeded modes, laminar flow design based on this technique intrinsically demands integrated prediction methods that go beyond the linear stability correlations typically employed in the context of other laminar flow control techniques. With that in mind, this paper attempts to include the linear and nonlinear growth of primary crossflow modes along with the linear amplification of high-frequency secondary instabilities towards more holistic predictions of the transition behavior. Section 3 describes the application of an N-factor criterion based on secondary instabilities of stationary crossflow modes to realistic flow configurations designed for DREs. These examples highlight the critical need to achieve a balance between sufficiently large and not-too-large control inputs for the successful implementation of the DRE technique in higher Reynolds number flows, as well as illustrating how such balance might be achieved via higher fidelity analyses techniques. Finally, some of the remaining challenges in applying such techniques are also pointed out.

## II. Roughness-Induced Tripping in High-Speed Boundary Layers

*A. Spanwise Periodic Trip Array on Hyper-X Forebody*

The computations described herein model the Hyper-X Mach 6 flow configuration from Ref. [12] at a nominal unit Reynolds number of Re = 2.2 x $10^6$/ft. The 0.333 scale forebody model tested in these experiments is 28 inches long, with a trip insert location at 7.4 inches from the leading edge. The model geometry consists of a rounded leading edge with a nose radius of 0.01 inches, followed by three flat ramps providing discrete, sequential, non-isentropic flow compressions ahead of the engine. At the nominal angle of attack equal to 2 degrees, the local compression angles for the three ramps correspond to 4.5, 5.5, and 3 degrees, respectively. The first compression corner (between ramps 1 and 2) is located at 12.4 inches, and the second corner at 17.7 inches. Of the various trip configurations tested in the experiment, trip configuration 2c (Fig. 1) was identified as providing the best combination of tripping effectiveness and reduced axial vorticity within the turbulent flow approaching the inlet. The results presented herein correspond to a trip spacing of $\delta$ = 0.081" and a peak height of h = 0.060". The latter trip height was sufficient to promote transition fairly close to the trip location in the experiment. Although the trip spacing for the computations described herein is smaller than the 0.12" spacing in Ref. [12], a comparison of computations for both trip spacing cases showed similar results as discussed in Ref. [8].

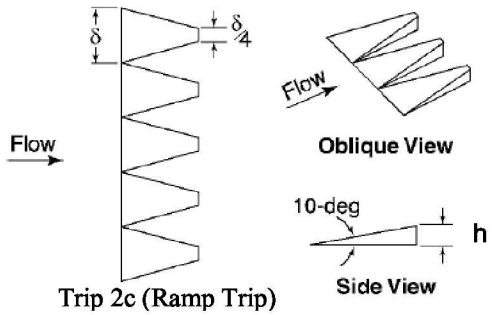


Figure 1. Schematic of trip configuration 2c (reproduced from Ref. [8]). Here, $\delta$ denotes the array spacing and h represents the maximum height of a trip element.

To obtain the mean-flow solution in the presence of the trip array, the compressible Navier-Stokes equations are solved using either global or local time stepping in conjunction with an implicit technique and 4th order discretization of advection terms. The immersed boundary (IB) technique [13] is used to simulate the effects of the trip array on the surrounding flow.

The spanwise varying boundary layer displacement due to the trip elements results in the formation of strong streamwise streaks in the wake of the trip array (Fig. 2). The velocity contours at several streamwise stations reveal that the streaks would persist for long distances over the forebody surface if the boundary-layer flow were to remain laminar throughout that region. The presence of longitudinal streaks behind the trip array was also noted in the conventional facility experiments by Berry et al. [14] as well as in the more recent measurements by Borg et al. [10] on the X-51A model, a configuration similar to Hyper-X, which was tested under both quiet and noisy conditions. The computations also indicate a rapid increase in streak amplitude across the compression corner (Fig. 3), a finding that is in qualitative agreement with the measurements in [14].

The stability characteristics of the roughness wake are examined next, with the goal of understanding whether the onset of transition behind the trip array may be related to the amplification of instability modes supported by the abovementioned streaks. Since the spanwise and wall-normal length scales of these streaks are comparable with each other, the modified boundary-layer flow has a strongly inhomogeneous character in both $y$ and $z$ directions. Therefore, its stability characteristics are more appropriately studied by solving a 2D eigenvalue problem, rather than using the conventional linear stability analysis, which is based on the assumption of basic state inhomogeneity along just the surface normal direction.

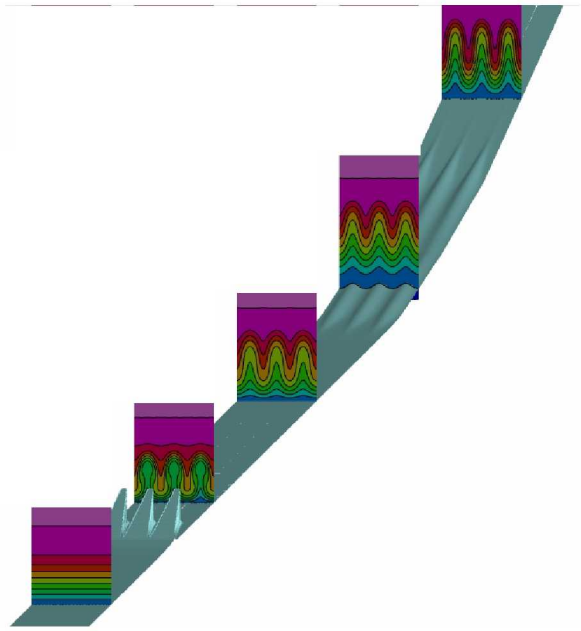

Figure 2. Streamwise streaks produced by trip array (visualized via u-velocity contours at $x$ = 6", 8", 10", 12", and 14", respectively; flow is from bottom left to upper right and, for visual clarity, the wall normal and spanwise coordinates $y$ and $z$ have been magnified relative to the $x$ coordinate). The underlying light blue surface corresponds to the isosurface of streamwise velocity for u=1m/sec.

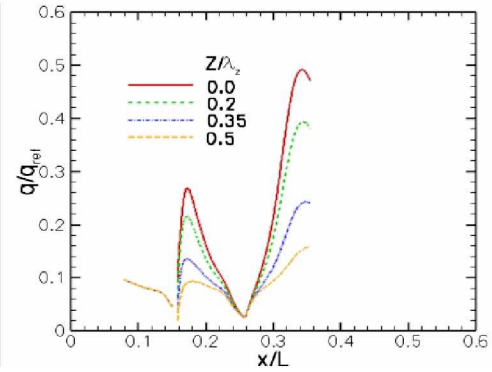


Figure 3. Predicted heat flux distribution at selected spanwise planes (indicated as a fraction of the array wavelength $\lambda_z$.) The streamwise extent of the trip array has been excluded from the plot. The abscissa has been normalized by the reference length of vehicle at the model scale, L = 48", and the ordinate has been normalized to provide an approximate match between the predicted heating near $x$/L=0.08 with the corresponding laminar value from [12].

As is typical of the boundary-layer flows modified by finite amplitude streaks [10, 15], multiple modes of instability tend to co-exist at a given station. The growth rates of the two dominant modes of instability at $x$ = 7.9" (i.e., in the near wake of the trip array) have been plotted against the disturbance frequency in Fig. 4(a), which also indicates the representative mode shapes for the magnitude of the u-velocity perturbation associated with each mode. The spanwise wavelength of these modes is equal to the array spacing $\delta$. Despite the presence of strongly inflexional boundary-layer profiles in the wall-normal direction, the more unstable mode (i.e., mode 1) from abovementioned modes is found to be driven by the spanwise ($z$) shear of the basic state (i.e., corresponds to an *odd* mode, which induces sinuous motions of the underlying stationary streaks). Since the spanwise shear occurs solely because of the trip array, this dominant, *odd* (or "$z$") mode of streak instability would not have existed without the roughness elements. The subdominant mode 2 is found to be an *even* mode that is primarily driven by the wall-normal ($y$) shear associated with the basic state.

Streamwise variation of growth rates and cumulative amplification ratios (N-factors) of fixed frequency disturbances belonging to each mode has been plotted in Figs. 4(b) and 4(c), respectively. As seen from Figs. 4(b)-(c), the growth of streak instabilities over model ramp 1 (both odd and even modes) ceases well upstream of the end of this ramp (x=12.4") before resuming again over the second compression ramp. The absence of growth in the immediate vicinity of the compression corner is attributed to the rapid decrease in streak amplitudes just ahead of the corner (Fig. 2). As seen from Fig. 4(c), the odd mode (mode 1-$z$) disturbances near f = 90 kHz reach an N-factor of approximately 7 across an amplification region of just 2.5 inches (which, however, is more than 7 times larger than the trip length). In a previous set of experiments in the same facility [16], transition onset on a smooth, flared cone model had been found to correlate with N≈4. Thus, if a similar value of N is assumed to correlate with the onset of roughness-induced transition on the Hyper-X model, then the predicted onset of transition will be within a distance of $\Delta x$/L = 0.05 behind the trip (where L=48" denotes the reference length of the vehicle at the model scale). This

prediction agrees with the phosphor thermography measurement in the experiment [12] which, too, is suggestive of transition onset at a short distance behind the trip array.

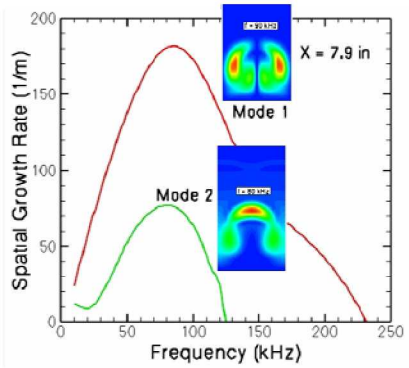


(a) Growth rates and representative modes shapes (based on the magnitude of streamwise velocity perturbation) at a fixed station ($x$=7.9").

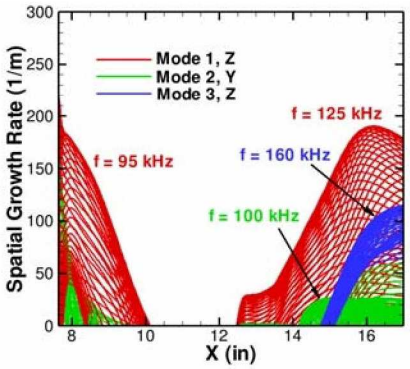


(b) Growth rates of fixed-frequency disturbances as functions of $x$. (Each curve denotes a specific frequency from the range of unstable frequencies corresponding to a given mode.)

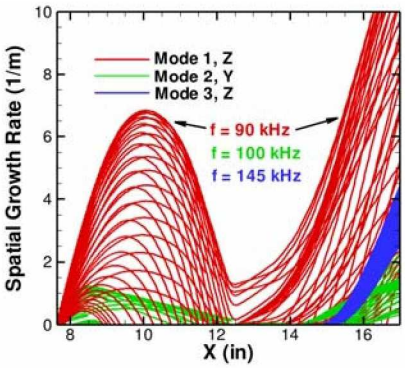


(c) Integrated logarithmic amplification ratios (N factors) for fixed frequency disturbances.

Figure 4. Instability characteristics of stationary streaks due to roughness array (The $y$-$z$ classification in parts b and c indicates the direction of basic state shear that is primarily responsible for the destabilization of a given mode.)

One may observe that the peak N-factor over the second compression ramp is significantly larger than that over model ramp 1 due to a longer region of disturbance amplification; however, this stronger growth may or may not be relevant in practice depending on whether transition already occurs over ramp 1 region. Because of the intervening region of strong decay in between the regions of growth on ramps 1 and 2, it is also possible to encounter somewhat abrupt variations in the transition location as the trip, flow, or facility parameters are varied [17].

*B. Isolated Roughness Element in a Mach 3.5 Flat Plate Boundary Layer*

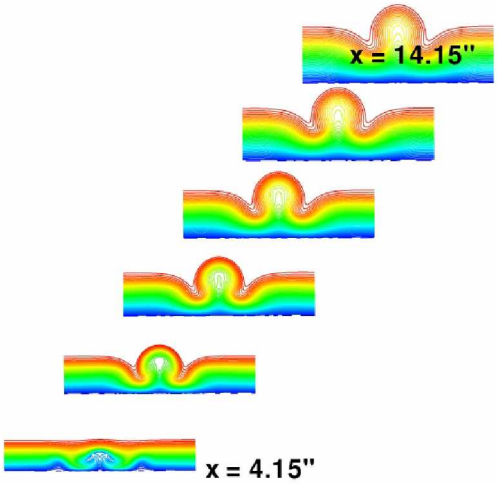


Fig. 5. Streamwise velocity contours behind an isolated, diamond trip of height 0.02 inches ($h/\delta^* \approx 0.73$, where $\delta^*$ denotes the displacement thickness of the boundary layer) in a Mach 3.5 flat plate boundary layer.

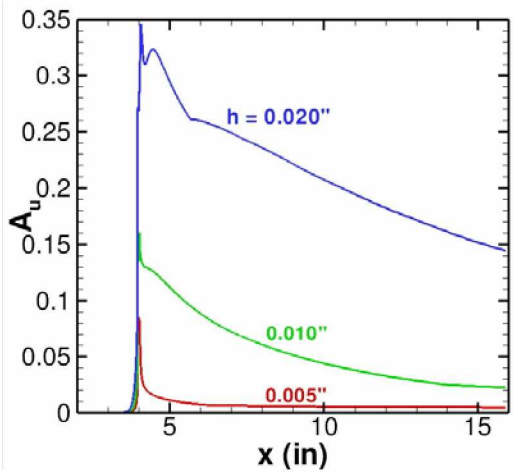


Fig. 6. Effect of trip height on streak amplitudes behind an isolated, diamond shaped trip element in Mach 3.5 boundary layer.

To further understand the effect of the compression corner, the case of an isolated trip without the destabilizing influence of a compression corner is examined next. Ccomputations similar to those for the Hyper-X trip array were performed for an isolated diamond trip mounted on a flat plate at zero incidence to the incoming free stream (Fig. 5). The flow conditions for these computations (M=3.5, Re=3x$10^6$/ft, T=90.2 deg K, width of each face of diamond trip = 0.05 inches) were chosen to be relevant to a planned experiment in the Supersonic Low Disturbance Tunnel at NASA Langley Research Center.

As shown in Fig. 6, streak amplitudes for the flat plate case decay nearly monotonically with distance from the trip (or the trip array), in contrast to the case of Hyper-X like compression surfaces where the rapid increase in streak strength near the compression corner helped sustain the strong streak amplitudes over large distances (Fig. 3). Fig. 6 also shows that the streak amplitudes have a strongly nonlinear dependence on the roughness height, not unlike the case of roughness-induced streaks in low-speed flows [18, 19]. Thus, no streak instabilities of the type discussed earlier are expected to exist behind the shallowest trip of height 0.005", whereas sufficiently strong wake instability is predicted to occur behind the trip element with the largest height.

*c. Parameter Study for Isolated Roughness Element in a Flat Plate Boundary Layer*

Additional computations have been carried out for both 2D and 3D roughness elements at other Mach numbers using the unstructured grid code EZ4D [9]. The 2D computations at subsonic Mach numbers reveal the presence of vortex shedding at sufficiently large roughness heights, which is suggestive of an absolute instability in the region of separation near the roughness element. The vortex shedding process weakens with increasing subsonic Mach number and no visibly obvious shedding was observed in the context of 2D computations at supersonic Mach numbers. Of course, the dominant instability modes at supersonic Mach numbers are known to be three-dimensional. Yet, as described below, no strong shedding was noted even in 3D, supersonic computations at roughness height Reynolds numbers that would have resulted in shedding in low-speed boundary layers.

Figure 7 shows the numerical Schlieren picture for a Mach 9.65 flow impinging on a flat plate with a cylindrical roughness element at approximately 3 inches from the sharp leading edge. The free-stream and wall temperatures are 53.3 K and 308 K, respectively. The plate is at an angle of attack equal to 20 deg, and the post shock Mach number is 4.16. The diameter and height of the cylindrical roughness element are equal to 4 mm and 2 mm, respectively. Time accurate Navier-Stokes computations were performed for two different stagnation pressures at which experiments have been performed at NASA Langley [20]. The corresponding Reynolds numbers based on post-shock unit Reynolds number and the height of the roughness element are approximately 6800 and 14300, respectively. Using the Sutherland law for viscosity, the roughness height to the boundary layer thickness ratio is nearly 1.3 and 2.8, respectively.

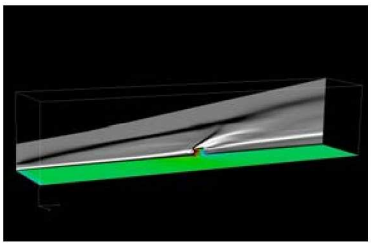

Figure 7. Numerical Schlieren picture at the symmetry plane and surface pressure contours for a Mach 9.65 flow over a cylindrical roughness element.

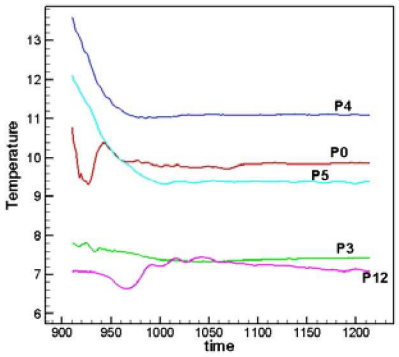


Figure 8. Time history of temperature variation at five arbitrary probe locations around the cylindrical roughness element at the lower Reynolds number of 6800 (Both abscissa and ordinate are suitably nondimensionalized.)

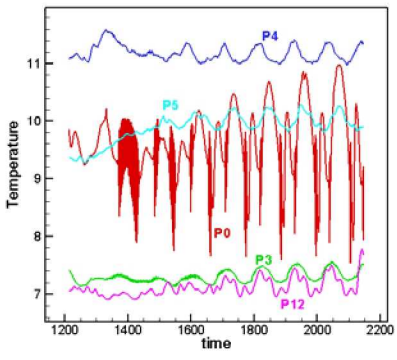


Figure 9. Time history of temperature variation at five different probe locations around the cylindrical roughness element at the higher Reynolds number of 14300.

Figures 8 and 9 display the time history of temperature variations at five arbitrary probe locations within the boundary layer for the low and high Reynolds number cases, respectively. At the lower Reynolds number, the flow eventually approaches a near steady-state behavior, even though some weak oscillations that are not visible on the scale of Fig. 8 may still be present. On the other hand, strong flow unsteadiness as shown in Fig. 9 is observed in the higher Reynolds number case, although the behavior of the unsteady flow appears to be different from the vortex shedding at subsonic Mach numbers. Both of these computations were done using the same grid and numerical dissipation parameters. However, because of the somewhat thinner boundary layer at the higher Reynolds number, the effective grid resolution is proportionally less. Thus, a grid convergence study will be performed in future to confirm the unsteady results in Fig. 9. However, the comparison between the above two cases does indicate that the flow around the same roughness element can sustain stronger, self-sustained unsteadiness when the Reynolds number and the effective roughness height exceeds certain threshold values.

## III. Control of Crossflow Transition in Subsonic and Supersonic Boundary Layers via DREs

As alluded to in the introduction, determination of appropriate control input parameters (e.g., wavelength and amplitude of the control mode) is one of the major issues in designing an effective laminar flow control system based on distributed roughness elements (DREs). Specifically, the control input must be large enough to provide the desired control action (viz., sufficient modification of the basic state to reduce the growth of the "dangerous" modes), however, it cannot be excessively large as to precipitate premature transition (and, hence, reduce the extent of the transition delay). As will be shown below, the secondary instability analysis (in conjunction with linear and nonlinear development of the primary instability in the form of stationary crossflow modes) can provide useful guidance for selecting an appropriate range of control input amplitudes. Computational results are presented for two specific configurations, *viz.*, transition control over (1) a 73-deg swept airfoil at Mach 2.4 and chord Reynolds number of $Re_c = 16 \times 10^6$ [21] and (2) a subsonic, 31-deg swept airfoil at -4.69 deg angle of incidence and $Re_c \approx 7 \times 10^6$ [1].

### *A. Case 1: Supersonic Boundary Layer*

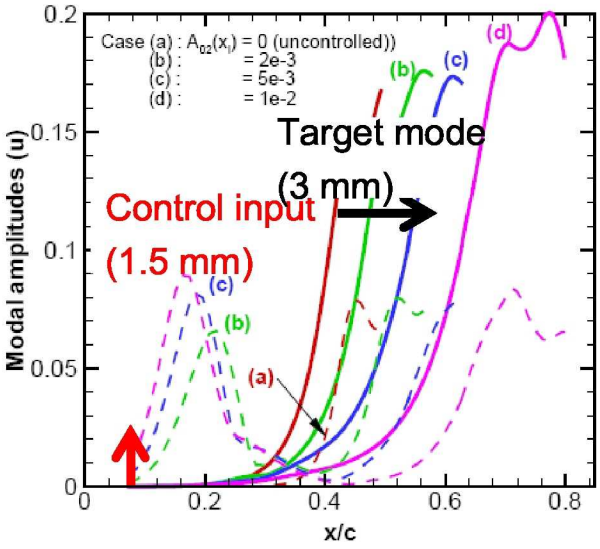


Figure 10. Mach 2.4 supersonic swept wing configuration: nonlinear control of most unstable mode ($\lambda_z$ = 3 mm) via control input with different initial amplitudes of $\lambda_z$ = 1.5 mm mode (from Ref. [22])

In case (1), the linearly most unstable stationary crossflow mode has a spanwise wavelength of approximately $\lambda_z$ = 3 mm [21, 22]. To simulate DRE based control in the simplest context, the less unstable first harmonic at $\lambda_z$ = 1.5 mm is introduced with the expectation that the earlier dominance of this shorter wavlength mode will reduce the initial growth of the target 3 mm mode via nonlinear effects. The effect of varying the height of the periodically spaced roughness elements at $\lambda_z$ = 1.5 mm is simulated by varying the initial amplitude of the control mode. Computations based on nonlinear parabolized stability equations (PSE) using NASA's LASTRAC code [22, 23] show that the region of rapid rise in the target mode amplitude can be pushed back progressively farther downstream via a control mode with sufficiently large initial amplitude (Fig. 10). Computations of secondary instability confirm the accompanying delay in the amplification of the secondary instability modes at $\lambda_z$ = 3 mm.

More interestingly, however, the secondary instability analysis at the control mode wavelength ($\lambda_z$ = 1.5 mm) reveals the increased likelihood of precipitating premature transition via overcontrol (i.e., unduly large control input) at the relatively large chord Reynolds number of interest. N-factor curves corresponding to the amplification of the relevant families of secondary instability modes are shown in Figs. 11(a) and 11(b) for initial control mode amplitudes of $\mathbf{A_i}$ = 0.001 and $\mathbf{A_i}$ =0.002, respectively. Similar to the streak instabilities described in Section 2, the high-frequency secondary

instability modes of stationary crossflow vortices can be usually classified as *y*-modes (i.e., modes driven by the wall-normal gradients of the basic state as modified by the control input), *z*-modes (i.e., mode associated with spanwise gradients), or as a mixture of the two. Even though a family of *z*-modes becomes unstable at an earlier location than the *y*-modes in Figs. 11(a)-(b), it is one of the *y*-modes that is predicted to have the highest amplification ratio at both values of the control input.

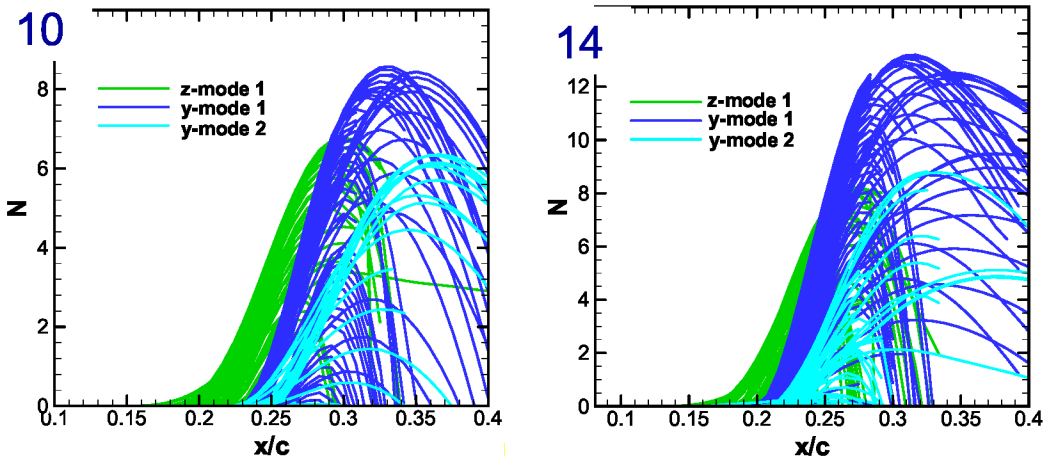


(a) **N-factors curves, $A_i = 0.001$** (b) **N-factors curves, $A_i = 0.002$**

Figure 11. Secondary instability of stationary crossflow mode at $\lambda_z = 1.5$ mm. (Different curves of the same color denote disturbance modes at different frequencies corresponding to a specific family of modes. The classification of mode families is analogous to that in Fig. 4.)

Due to the rapid growth of the secondary instability modes, an N-factor criterion based on the envelope of the amplification curves in Fig. 11 would appear to provide a relatively sensitive indicator for transition onset. However, previous experience [15, 24] suggests that, in certain cases, the *z*-modes would be more likely to be observed in an experiment even if they may not have the largest N-factors. In light of this observation, the N-factor envelopes for the *y* and *z* families of modes, respectively, were examined separateky. The relatively large N-factors for both *y*- and *z*-modes in Figs. 11(a)-(b) suggest that premature transition in the vicinity of 30 percent chord would be a distinct possibility, especially at $A_i = 0.002$, regardless of whether or not the more unstable *y*-modes are realized in practice.

*B. Case 2: Subsonic Boundary Layer*

In case (2), similar analyses have been carried out for the low speed configuration that was tested during a recent flight experiment [1]. The target mode wavelength is 4.5 mm, whereas the control mode corresponds to $\lambda_z = 2.25$ mm. Again, nonlinear PSE computations [11] confirm the weakening of target mode amplitudes via a control mode of sufficiently large initial amplitude (Fig. 12(a)). However, the extent of stabilization is not monotonic with respect to the control input magnitude, presumably due to its dependence on the relative phase of the two modes [22] in this particular case.

Computations of secondary instability also reveal the accompanying reduction in the amplification of both *y* and *z* families of secondary instability modes at the target mode wavelength. Even though the *z*-modes are dominant in the absence of the control input, they are much more strongly stabilized in the presence of the control input and the resulting N-factors at farther downstream stations are much smaller than those of the *y*-modes. Given this disparity in the effects of the control input on the two types of secondary instability modes at the target mode wavelength, along with the previously mentioned ambiguity in whether or not the *y*-type secondary modes should be used for transition correlation, it becomes difficult to quantify the extent of transition delay in the present case using the secondary N-factor criterion. Yet, Fig. 12(b) seems to indicate that a lower bound on the extent of transition delay could still be obtained on the basis of the downstream shift in the overall N-factor envelope (i.e., based on simultaneous consideration of both modes of secondary instability). It is also useful to mention that the effect of control input on the relative growth of *y*- and *z*-modes of secondary instabilities is roughly analogous to the effect of

lowering the initial amplitude of the target mode in the no-control case. In the course of engineering analyses, it might be possible to exploit this similarity by limiting the relatively expensive secondary instability calculations to a basic state that is based on the nonlinear evolution of the target mode alone at various initial amplitudes (i.e., with zero control input).

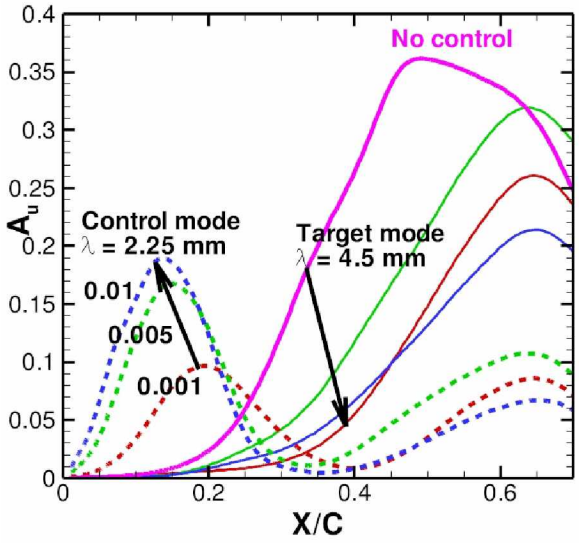


Figure 12(a) Modal amplitude evolution of linearly most unstable stationary crossflow mode ($\lambda_z$ = 4.5 mm) in the presence of control input at $\lambda_z$ = 2.25 mm

The uncertainty related to whether both *y*- and *z*-modes of secondary instability or just the *z*-modes should be used for N-factor correlation also has an impact on predicting the potential for overcontrol in case (2). Specifically, secondary instability analysis at the control mode wavelength indicates that the *z*-modes at $\lambda_z$ = 2.25 mm have rather small N-factors at both $A_i$ = 0.005 and 0.01, but that the *y*-modes can reach N-factor values exceeding 9 for the larger control input. Thus, whether or not premature transition due to unduly large control input will occur in that case would depend on the realizability and receptivity characteristics of the *y*-modes [25]. The latter issues cannot be directly addressed in the course of the flight experiment [1]; however, measurements of the crossflow disturbance amplitudes, together with simultaneous measurements of transition onset could provide sufficient data to help reduce the associated uncertainty in applying a secondary N-factor criterion to other similar configurations.

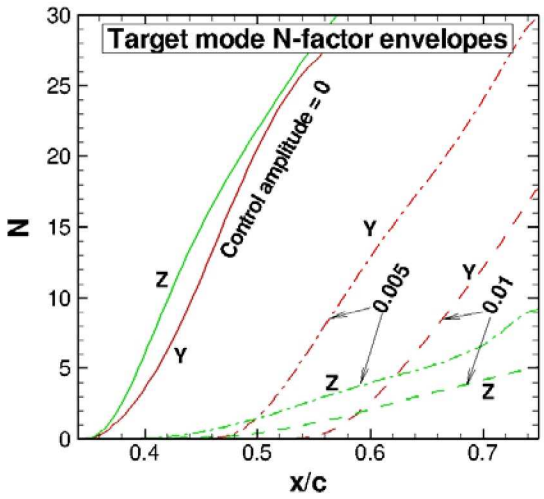


(b) N-factor envelopes for dominant *y*- and *z*-mode secondary instabilities with $\lambda_z$ = 4.5 mm for initial control mode amplitudes of $A_i$ = 0, 0.005, and 0.01.

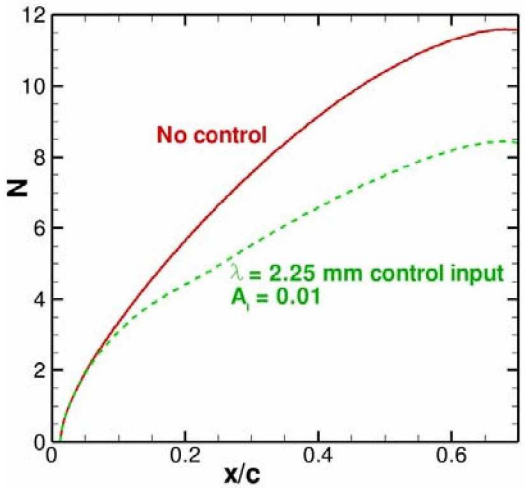


(c) Linear growth of λ = 4.5 mm stationary crossflow mode with and without mean flow correction due to control input (Initial amplitude $A_i$ = 0.01)

Figure 12. DRE based laminar flow control on the subsonic, SWIFT flight configuration [1].

Finally, to explore a computationally easier alternative to secondary instability analysis in the context of DREs, Fig. 12(c) examines the linear stability of the spanwise averaged flow in the presence of the nonlinear distortion due to the control input. Specifically, it compares the N-factor values for the target mode as predicted via linear instability analysis of the spanwise averaged mean flow without and with the control input. The figure shows that the basic state modification due to the control mode results in a significant reduction in the peak N-factor relative to the

uncontrolled case ($\Delta N \approx 3.2$ near x/c=0.6). However, additional work is necessary to establish whether and how such simplified analysis may be applied towards the design of DREs.

## IV. SUMMARY

By applying artificial roughness elements, boundary layer transition can be either hastened or delayed, depending on the specific requirements for flow control. In the case of boundary layer tripping over a compression surface ahead of the engine inlet on a hypersonic air-breathing configuration, roughness elements generate stationary streaks that amplify across the compression corner and, furthermore, enhance the growth of non-stationary streak instabilities that are expected to trigger an earlier transition as observed in the experiments. In the case of crossflow transition delay via distributed roughness elements, carefully designed roughness elements produce subdominant crossflow vortices that reduce the growth of the naturally dominant crossflow modes and hence weaken the high frequency secondary instabilities that would have otherwise led to an earlier onset of transition. The 2D eigenvalue computations of secondary instabilities can play an important role in the analysis of DRE based laminar flow control by delineating an optimal range of control input magnitude and, hence, providing approximate bounds on the extent of transition delay achievable through the DREs.

### Acknowledgments

The work of NASA authors has been performed as part of Subsonic Fixed Wing, Supersonics, and Hypersonics Projects of NASA's Fundamental Aeronautics Program (FAP). The work of Prof. Edwards has been funded under the AFOSR grant FA9550-0701-0191. The authors thank Dr. Mujeeb Malik and Mr. Scott Berry for useful technical discussions.

### References

1. Carpenter, A.L., Saric, W.S., and Reed, H.L., "Laminar Flow Control on a Swept Wing with Distributed Roughness," AIAA Paper 2008-7335, 2008.
2. Saric, W. S., Carillo, R. B., and Reibert, M. S., "Leading Edge Roughness as a Transition Control Mechanism," AIAA Paper 98-0781, Jan. 1998.
3. Crouch, J.D., "Modeling Transition Physics for Laminar Flow Control," AIAA Paper 2008-3832, 2008.
4. Klebanoff, P., Cleveland, W.G., and Tidstrom, K.D., "On the Evolution of a Turbulent Boundary Layer Induced by a Three-Dimensional Roughness Element," J. Fluid Mech., Vol. 237, pp. 101-187, 1992.
5. Reshotko, E. and Tumin, A., "Investigation of the Role of Transient Growth in Roughness-Induced Transition," AIAA Paper 2002-2850, 2002.
6. Morkovin, M. V., "Panel Summary on Roughness," *Instability and Transition*, edited by M. Y. Hussaini and R. G. Voight, Vol. 1, Springer-Verlag, Berlin, 1990, pp. 265–271.
7. Schneider, S.P., "Effects of Roughness on Hypersonic Boundary-Layer Transition," AIAA Paper 2007-305, 2007
8. Choudhari, M., Li, F., and Edwards, J.A., "Stability Analysis of Roughness Array Wake in a High-Speed Boundary Layer," AIAA Paper 2009-0170.
9. Chang, C.-L., and Choudhari, M., "Hypersonic Viscous Flow over Large Roughness Elements," AIAA Paper 2009-0173, 2009.
10. Li, F., and Choudhari, M., "Spatially Developing Secondary Instabilities and Attachment Line Instability in Supersonic Boundary Layers," AIAA Paper 2008-590, 2008.
11. Li, F., Choudhari, M., Chang, C.-L., Streett, C.L., and Carpenter, M., "Roughness Based Crossflow Transition Control: A Computational Assessment," AIAA Paper 2009-4105 (To appear).
12. Berry, S.A., Auslender, A.H., Dilley, A.D., and Calleja, J.F., "Hypersonic Boundary-Layer Trip Development for Hyper-X," J. Spacecraft and Rockets, vol. 38, No. 6, pp. 853-864, Nov.-Dec. 2001.
13. Ghosh, S., Choi, J.-I., and Edwards, J.R. "RANS and hybrid LES/RANS Simulation of the Effects of Micro Vortex Generators using Immersed Boundary Methods" AIAA Paper 2008-3728, June, 2008
14. Borg, M.P., and Schneider, S.P., "Effect of Freestream Noise on Roughness-Induced Transition for the X-51A Forebody," AIAA Paper 2008-592, 2008.
15. Malik, M. R., Li, F. Choudhari, M. M. and Chang C.-L., "Secondary Instability of Crossflow Vortices and Swept-wing Boundary-layer Transition." J. Fluid Mech. Vol. 399, 1999, pp. 85- 115.
16. Horvath, T. J., Berry, S. A., Hollis, B. R., Chang, C.-L., and Singer, B. A., "Boundary Layer Transition On Slender Cones In Conventional and Low Disturbance Mach 6 Wind Tunnels," AIAA Paper 2002-2743, 2002.
17. Berry, S.A., Nowak, R., and Horvath,, T.J., "Boundary Layer Control for Hypersonic Airbreathing Vehicles," AIAA Paper 2004-2246, 2004.
18. White, E.B., and Ergin, F.G., "Receptivity and Transient Growth of Roughness-Induced Disturbances," AIAA Paper 2003-4243, 2003.
19. Choudhari, M. and Fischer, P., "Roughness-Induced Transient Growth" AIAA Paper 2005-4765, 2005.

20. Danehy, P.M., Garcia, A.P., Borg, S., Dyakonov, A.A., Berry, S.A., Inman, J.A., and Alderfer, D.W., "Fluorescence Visualization of Hypersonic Flow Past Triangular and Rectangular Boundary-Layer Trips," AIAA Paper 2007-536, 2007.
21. Saric, W., and Reed, H.L., "Supersonic laminar flow control on swept wings using distributed roughness." AIAA paper 2002-147, 2002.
22. Choudhari, M, Chang, C.-L., and Jiang, L., "Towards Transition Modeling for Supersonic Laminar Flow Control," Philosophical Transactions of Royal Society of London (Physical and Mathematical Sciences), vol. 363, no. 1830, pp. 1041-1259, 2005.
23. Chang, C.-L., "Langley Stability and Transition Analysis Code (LASTRAC) Version 1.2 User Manual," NASA/TM-2004-213233, June, 2004.
24. White E. B., and Saric W. S., "Secondary Instabilty of Crossflow Vortices." J. Fluid Mech. Vol. 525, pp. 275-308, 2005.
25. Bonfigli, G, and Kloker, M., "Secondary Instability of Crossflow Vortices: Validation of the Stability Theory by Direct Numerical Simulation," J. Fluid Mech., Vol. 583, pp. 229-272, 2007.